Preprint Cambridge Centre for Computational Chemical Engineering ISSN 1473 – 4273

Numerical simulation and parametric sensitivity study of optical band gap in a laminar co-flow ethylene diffusion flame

Edward K. Y. Yapp[1], Robert I. A. Patterson[2], Jethro Akroyd[1], Sebastian Mosbach[1], Erin M. Adkins[3], J. Houston Miller[3], Markus Kraft[1,4]

released: 5 October 2015

[1] Department of Chemical Engineering
and Biotechnology
University of Cambridge
New Museums Site
Pembroke Street
Cambridge, CB2 3RA
United Kingdom
E-mail: mk306@cam.ac.uk

[2] Weierstrass Institute for Applied
Analysis and Stochastics
Mohrenstraße 39
Berlin 10117
Germany

[3] Department of Chemistry
George Washington University
Washington, DC 20052
United States
E-mail: houston@gwu.edu

[4] School of Chemical
and Biomedical Engineering
Nanyang Technological University
62 Nanyang Drive
Singapore 637459

Preprint No. 159

UNIVERSITY OF CAMBRIDGE

Keywords: Soot, PAH, Optical band gap, OBG, Modelling, Diffusion flame

Edited by
Computational Modelling Group
Department of Chemical Engineering and Biotechnology
University of Cambridge
New Museums Site
Pembroke Street
Cambridge CB2 3RA
United Kingdom

Fax: + 44 (0)1223 334796
E-Mail: c4e@cam.ac.uk
World Wide Web: http://como.cheng.cam.ac.uk/

Highlights

- Modelling of optical band gap (OBG) of polycyclic aromatic hydrocarbons (PAH)
- PAHs in the gas phase absorbing light at the visible wavelength used for extinction measurements
- Results consistent with critical PAH size for inception of about 16 aromatic rings

Abstract

A detailed population balance model is used to perform a parametric sensitivity study on the computed optical band gap (OBG) of polycyclic aromatic hydrocarbons (PAHs) in a laminar co-flow ethylene diffusion flame. OBG may be correlated with the number of aromatic rings in PAHs which allows insights into which are the key species involved in the formation of soot. PAH size distributions are computed along the centerline and in the wings of the flame. We compare our simulations with experimentally determined soot volume fraction and OBG (derived from extinction measurements) from the literature. It is shown that the model predicts reasonably well the soot volume fraction and OBG throughout the flame. We find that the computed OBG is most sensitive to the size of the smallest PAH which is assumed to contribute to the OBG. The best results are obtained accounting for PAH contribution in both gas and particle phases assuming a minimum size of ovalene (10 rings). This suggests that the extinction measurements show a significant absorption by PAHs in the gas phase at the visible wavelength that is used, which has been demonstrated by experiments in the literature. It is further shown that PAH size distributions along the centerline and in the wings are unimodal at larger heights above burner. Despite the different soot particle histories and residence times in the flame, the PAH size associated with both modes are similar which is consistent with the near-constant OBG that is observed experimentally. The simulations indicate that the transition from the gas phase to soot particles begins with PAHs with as few as 16 aromatic rings, which is consistent with experimental observations reported in the literature.

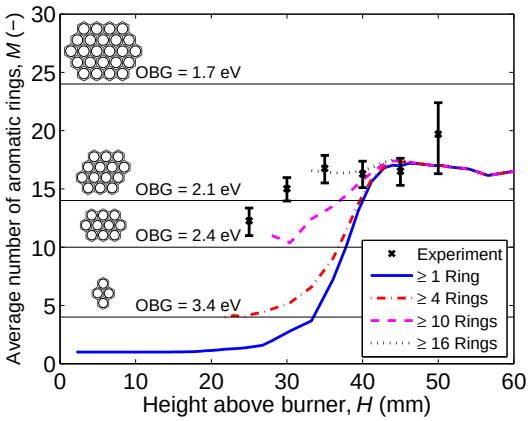

Contents

1 Introduction

Particle inception is the least understood process of soot formation in hydrocarbon combustion. It is widely accepted that the gaseous precursors to solid soot particles are polycyclic aromatic hydrocarbons (PAHs) [17, 28, 30, 31]. These PAHs grow in size due to chemical reactions and then stick. Experimental evidence for the sticking of PAH comes, for example, from the laser ionization mass spectrometric study by Happold et al. [27]. Masses of molecular fragments ablated from soot in a 100-Torr ethylene-oxygen flame display a periodicity of about 450 amu. Combined with the quantum mechanical calculations [38] and Bragg reflexions [9] reported in the literature, these studies provide support that nascent soot is made up of stacks of PAHs. The next question that arises is at what point do PAHs stick? A systematic effort has been made in this direction using a variety of experimental techniques. The rapid insertion technique has been routinely employed (see, e.g., [11, 33, 46, 55]) to collect particles which can be subjected to ex situ analysis using Raman spectroscopy [3, 10, 29] and high resolution transmission electron microscopy (HRTEM) [3, 32] to characterise the crystalline structure of soot particles. Observed Raman signals for soot generated from a non-premixed ethylene/air flame, which interestingly only show a slight variation, are attributed to particulates with a crystallite length of 1.0–1.2 nm, or PAHs which are 4–5 rings across [29]. HRTEMs of soot in ethylene and benzene-air flames reveal structures composed of sheet-like PAH molecules referred to as lattice fringes [3]. The most common fringe length throughout either flame is found to be equivalent to the length of a PAH about 4 rings across. However, these techniques only reveal the length of the crystallite structures. In ref. [1] an entirely different approach is used where visible light extinction measurements in a series of non-premixed ethylene/air flames of varying dilution ratios are performed and used to determine the optical band gap (OBG) as a function of flame position which is then related to the number of aromatic rings in a PAH [39]. The observed OBG is found to correspond on average to a PAH consisting of about 14 aromatic rings [1].

Tauc et al. [61] related the absorption behaviour of germanium to the OBG, the energy required for an electronic transition between the top of the valence band and the bottom of the conduction band. The absorption edge of a semiconductor is described by the relation:

$$\alpha h\nu \approx (h\nu - E_{\mathrm{g}})^{r}, \tag{1}$$

where α is the absorption coefficient, $h\nu$ is the photon energy, E_{g} is the OBG and r is a constant related to the band structure. In amorphous semiconductors r is taken to be 2 for a nondirect transition. In crystalline semiconductors r describes both the directness and the allowedness of the transition. For the experimental results referenced in this work $r = 1/2$ for a direct allowed transition is utilized. A plot of $(\alpha h\nu)^{1/r}$ against $h\nu$ has a distinct linear regime; therefore, extrapolation of this region to the abscissa yields the OBG. Robertson and O'Reilly [49] showed that the OBG scales inversely with $M^{1/2}$, where M is the number of aromatic rings in a cluster. By calculating the highest occupied molecular orbital-lowest occupied molecular orbital energy gaps for a series of PAH molecules and fitting the results [39] to the relationship proposed by Robertson and O'Reilly [49], the following

relationship is obtained:

$$E_{\mathrm{g}} = \frac{5.8076}{M^{1/2}} + 0.5413. \tag{2}$$

Through this relationship the OBG derived from extinction measurements can be related to the number of aromatic rings in a PAH.

In modelling studies of soot particle dynamics the growth of PAHs up to infinite size can be modelled via H-abstraction-C_2H_2-addition reactions (HACA) [17, 18, 20], or in combination with the more recently proposed PAH-addition cyclisation, phenyl addition cyclisation and methyl addition cyclisation mechanisms (see ref. [42] and references therein), deterministically solving for the concentration of each PAH species is computationally intractable. There are other detailed models of soot formation and solution methods. Kraft and co-workers employ a detailed population balance model which is solved using a stochastic numerical method. The model describes particles as aggregates composed of primary particles which are in turn composed of individual PAHs, thus containing information on particle size, morphology, and the internal structure of the particles. The exact structure of each PAH is resolved; therefore, the exact number of aromatic rings in each PAH is known. The OBG can then be computed using Eq. (2) and compared with experimentally determined OBG. The model has been used to simulate the oxidation of soot by NO [51]. It is found that a number of N and O atoms on the PAH edge cannot be removed, specifically, those on phenalene-like structures. This indicates that the present mechanism for PAH oxidation requires some phenalene removal process to improve model predictions of soot oxidation. The stochastic approach has also been used to understand the collision efficiency of the sticking of PAHs, where computed mass spectra are compared with the experimental mass spectra of Happold et al. [26] which contain distinctive features resembling PAH monomers and dimers. A unique feature of the model is that it resolves the size and connectivity of the primary particles in an aggregate; therefore, TEM-like projections of aggregates can be produced to visualise the temporal evolution of the fractal dimension in different flames [40]. Investigations of soot particle size distribution functions, morphology and composition have been performed in the context of engines [41]. The stochastic approach is also used to follow the morphology of aerosols in Titan's atmosphere [34] and to study the sintering of titania, silica and silicon.

The **purpose of this paper** is to compare computed OBG with OBG derived from extinction measurements made in a laminar co-flow ethylene diffusion flame [1], to understand the implications on the critical PAH size for soot inception, and to add jump processes to the kinetic Monte-Carlo-aromatic site (KMC-ARS) submodel. The flame chemistry and structure are taken from Herdman et al. [29] who employ an axisymmetric model which solves the full set of transport equations and we apply a soot population balance model in a postprocessing step. A parametric sensitivity study is carried out to understand how key model parameters impact the OBG quantitatively and to aid in the interpretation of the OBG.

The paper is organised as follows: Section 2 introduces the computational method. Section 3 introduces key aspects of the detailed population balance model, and the jump processes that are added to the KMC-ARS submodel. Section 4 contains a description of the direct simulation algorithm (DSA) used in this work and the changes that are made to

the algorithm. Sections 5.1 and 5.2 present the soot volume fraction and OBG, respectively. Section 5.3 presents the parametric sensitivity study of the computed OBG. Lastly, implications on the underlying simulations are discussed in Section 6.

2 Computational method

The computational method consists of two parts. In the first part, velocity, species and temperature fields for a laminar co-flow ethylene diffusion flame are taken from Herdman et al. [29]. They employ an axisymmetric model which has been developed by Smooke and co-workers [12, 35, 57–59] which solves the full set of mass, momentum, species and energy equations as well as the soot transport equations using a sectional representation of the soot particle size distribution [23]. A gas-phase chemical mechanism, and species thermodynamic and transport properties are supplied as input. The transport equations of the discretised particle size distribution function approximately account for the production and consumption of key gas-phase species due to surface growth, oxidation and condensation processes. A total of 20 sections are used. Although the largest PAH species described by the chemical mechanism is benzene [60], steady-state expressions are derived for the formation rate of larger PAHs up to $C_{52}H_{49}$. The computed soot results are found to be relatively independent of the size of the largest PAH that is modelled. It is worth mentioning that the concentrations of benzene (A1) and acetylene (C_2H_2) along the centerline are measured and compared against model results [58]. These two species are critical to PAH mass growth through ring-ring condensation reactions [64] and HACA [19].

In the second part, streamlines are generated in the velocity vector field from a collection of seed points along the burner surface, where each streamline terminates when the velocity is effectively zero. In this work, a detailed population balance model is then applied as a post-processing step where the computed temperature and species profiles along each streamline are extracted from the results of Herdman et al. [29] and supplied as input. This two-step methodology has been applied to the studies of a number of laminar premixed flames [4, 7, 8, 44, 48, 53, 67] and ideal reactor simulations [2, 52].

3 Detailed population balance model

In this work, a detailed population balance model [8] is used to model soot formation by postprocessing full transport equation simulations of the co-flow diffusion flame. The growth of PAH species within the model is described by a kinetic Monte-Carlo-aromatic site (KMC-ARS) model [47], starting from benzene. The dynamics of the soot particle population is described by the Smoluchowski equation [21, 22, 56] with additional terms for particle inception, surface growth, oxidation, condensation and sintering. A brief description of the most important aspects of the particle model is given below. Further details may be found elsewhere [8, 47, 53].

In the model, soot particles are represented as aggregates composed of primary particles, where each primary particle is composed of a number of PAHs [53]. A PAH is repre-

sented by the number of carbon and hydrogen atoms it contains, and the number and types of elementary sites on its edge [47]. These elementary sites include free-edge, zig-zag, armchair and bay sites [6, 16]. This representation allows the exact structure of each individual PAH to be resolved. A primary particle is represented as a set of two or more PAHs. An aggregate is represented as a set of two or more primary particles. Each aggregate stores a list of neighbouring primary particles and resolves the common surface area between each pair of neighbours, where each pair of neighbours can be in point contact, can be fully coalesced or can be anywhere in between [53]. The level of coalescence is described by a *sintering level*, $c \in [0,1]$ [52]. A sintering level of 0 corresponds to point contact and a sintering level of 1 corresponds to complete coalescence.

There are five different particle processes in the model:

Inception A primary particle is formed when two PAH molecules stick following a collision. The rate of collision is determined by a transition regime coagulation kernel [44] which is dependent on the mass and collision diameter of each collision partner [67]. The sticking probability of these two PAHs is determined by a simple collision efficiency model [8]. In this work, if the number of 6-member aromatic rings in each of the collision partners exceeds 16, which provides the best agreement between the experimentally derived OBG and computed OBG, then they will stick. This implies a unit sticking probability. In the present paper, we test a more complex collision efficiency function [48] where different collision efficiencies are applied to different PAH species, however, the results are insensitive to this approach.

Coagulation An aggregate is formed when two (primary or aggregate) particles stick following a collision. The rate of collision is calculated as per the transition regime coagulation kernel. After a coagulation event, two primary particles (one from each collision partner) are assumed to be in point contact. These primaries may undergo subsequent particle rounding due to mass addition [53] via surface growth and condensation, and due to sintering [52].

Surface growth PAHs in a primary particle may grow via surface reactions with gas-phase species. The rate of surface growth is a function of the structure of the PAH and is described by the KMC-ARS model. Two parameters are introduced to differentiate the rate of growth of PAHs in a primary particle versus those in the gas phase: the growth factor, g, and the critical number of PAHs in a primary particle, n_{crit}. The *growth factor* $g \in [0,1]$ [53] is a multiplier that is applied to the growth rate of PAHs within primary particles once the number of PAHs (n_{PAHs}) exceeds n_{crit}. It is intended to account for the possibility that PAHs in large primary particles grow more slowly than PAHs in the gas-phase.

Surface growth increases the mass of a PAH, which results in an increase in the sphericity of the primary particle containing the PAH and any neighbouring primary particles [53]. This particle rounding takes the form of an increase in the common surface area between the affected primary particles. The rate of particle rounding is parameterised by a *smoothing factor* $s \in [0,2]$ [53] that relates the change of the common surface area to the change of the volume of a primary particle. A smoothing factor of 0 implies instantaneous coalescence, whereas a smoothing factor of 2 corresponds to no rounding.

Consistent with the inception process, if a surface reaction reduces the number of 6-member aromatic rings in a PAH in a particle (defined as $n_{\mathrm{PAHs}} \geq n_{\mathrm{crit}}$) below the inception threshold, the PAH is removed. The KMC-ARS model is comprised of 20 jump processes. While it contains the most important aspects of PAH growth and oxidation, it is incomplete. Detailed chemical mechanisms containing a large number of reaction to study the growth of large, non-planar PAHs have been developed by Whitesides and Frenklach [66] and Violi [63]. Perhaps the most interesting among them is capping of an embedded 5-member ring as it causes the PAH structure to curve. Incorporation of such jump processes into the KMC-ARS model is the subject of future work. With the present PAH reaction mechanism PAHs containing phenalene-like structures cannot be oxidised, such as the one shown in Fig. 1. In this paper we propose two PAH jump processes which allow for such structures to be oxidised:

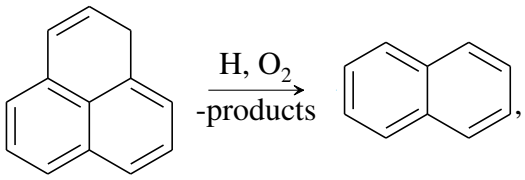

(3)

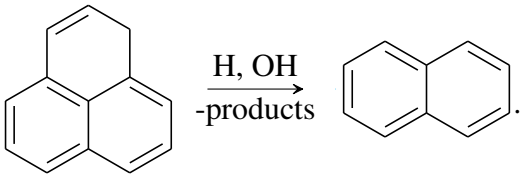

(4)

We estimate the rate of reactions 3 and 4 from the rate of analogous hydrogen abstraction and oxidation reactions on the free-edge site, reaction sequences S9 and S10, respectively, from ref. [47].

Condensation A particle may grow via condensation of a gas-phase PAH, following a collision between the PAH and a primary or aggregate particle. The rate of collision is calculated as per the transition regime coagulation kernel. Consistent with the inception process, if the condensing PAH has 16 or more 6-member aromatic rings, it will stick to the particle. Rounding by mass addition occurs via the same mechanism as described for the surface growth process.

Sintering Neighbouring primary particles may undergo particle rounding via a sintering process [36, 52, 65]. The rate of sintering between each pair of neighbouring primary particles p_i and p_j is given [52]:

$$\frac{\mathrm{d}C_{i,j}}{\mathrm{d}t} = -\frac{1}{\tau_{\mathrm{s}}}(C_{i,j} - S_{i,j}), \tag{5}$$

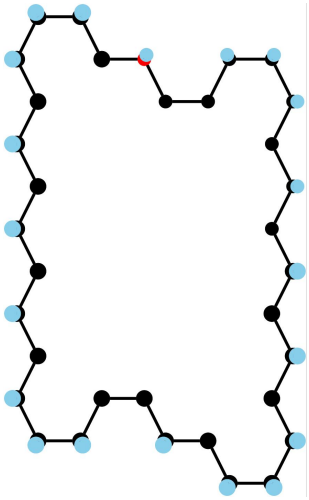

Figure 1: *Example of a computed PAH structure at the end of the simulation when there is no process by which phenalene-like structures can be removed.*

where $C_{i,j}$ is the common surface area of primary particles p_i and p_j, and $S_{i,j}$ is the surface area of a sphere with the same volume as primaries p_i and p_j. The characteristic sintering time is given [62]:

$$\tau_s = A d_{i,j} \exp\left[\frac{E}{T}\left(1 - \frac{d_{\text{crit}}}{d_{i,j}}\right)\right], \tag{6}$$

where A is the pre-exponential factor, $d_{i,j}$ is the minimum diameter of two neighbouring primary particles, E is the activation energy and d_{crit} is the critical primary particle diameter below which the primaries are assumed to be liquid-like and 'sinter' instantaneously.

The sintering level $c_{i,j}$ determines how far primary particles p_i and p_j have sintered:

$$c_{i,j} = \frac{\frac{S_{i,j}}{C_{i,j}} - 2^{-1/3}}{1 - 2^{-1/3}}, \tag{7}$$

where a value of 0 implies that the primary particles are in point contact, while a value of 1 means that the primary particles are fully sintered.

There are many parameters in the model, but the key parameters we investigate in this work are given in Table 1. Ranges within which these parameters are expected to vary and the initial values chosen for the base case simulations are shown. In ref. [8], the five parameters ρ, s, g, E and d_{crit} are optimised against the experimental PSDs for a set of laminar premixed ethylene flames [25].

Table 1: *Model parameters in detailed population balance model.*

Parameter (units)	Range	Value
1) Minimum number of 6-member aromatic rings in a PAH for inception	-	16
2) Minimum number of 6-member aromatic rings in a PAH for condensation	-	16
3) Minimum number of 6-member aromatic rings in a PAH in a particle ($n_{\mathrm{PAHs}} \geq n_{\mathrm{crit}}$) below which it is removed	-	16
4) Soot density, ρ	1 g cm^{-3} $\leq \rho \leq$ 2 g cm^{-3}	1.88 g cm^{-3}
5) Smoothing factor, s	$0 \leq s \leq 2$	1.69
6) Growth factor, g	$0 \leq g \leq 1$	0.0263
7) Critical number of PAHs in a primary particle before the growth factor is applied, n_{crit}	≥ 2	2
8) Sintering model:		
- A	-	1.1×10^{-14} s m^{-1}
- E	1.8×10^4 K $\leq E \leq 1.8 \times 10^5$ K	9.61×10^4 K
- d_{crit}	1 nm $\leq d_{\mathrm{crit}} \leq$ 5 nm	1.58 nm

4 Numerical method

In this work, direct simulation algorithm (DSA) [4, 14] is used to solve the detailed population balance equations. We introduce an approximation to the algorithm for reasons which will be explained later. Therefore, DSA and the various techniques - linear process deferment algorithm (LPDA) [43] and the concept of majorant kernels and fictitious jumps [13, 44] - that have been employed to enhance the performance of DSA warrant a brief explanation. The total rate of coagulation R using DSA is given by:

$$R = \frac{1}{2} \sum_{i \neq j}^{N(t)} K(P_q, P_r), \tag{8}$$

where $N(t)$ is the number of stochastic particles in the ensemble at time t and $K(P_q, P_r)$ is the kernel describing the rate of coagulation between two particles P_q and P_r. We use the popular transition kernel defined as:

$$K^{\mathrm{tr}}(P_q, P_r) = \frac{K^{\mathrm{sf}}(P_q, P_r) K^{\mathrm{fm}}(P_q, P_r)}{K^{\mathrm{sf}}(P_q, P_r) + K^{\mathrm{fm}}(P_q, P_r)}, \tag{9}$$

where $K^{\mathrm{sf}}(P_q, P_r)$ and $K^{\mathrm{fm}}(P_q, P_r)$ are the slip-flow and free-molecular kernels, respectively. It is computationally more efficient to evaluate the majorant kernel $\hat{K}$ as an approximation of the true kernel K such that $\hat{K} \geq K$. The distribution and rate defined by K is then

recovered by rejecting the selection of two particles P_q and P_r with probability [13, 44]:

$$1 - \frac{K(P_q, P_r)}{\hat{K}(P_q, P_r)}. \tag{10}$$

Where the preliminary selection is rejected it is referred to as a fictitious jump. LPDA is designed for problems where nonlinear particle processes cannot be neglected but the rate is dominated by linear processes, i.e., surface growth. In such cases LPDA has been shown to reduce computational times. With DSA, surface growth events are deferred and are performed on a pair of particles only once the particle pair is selected for inception, coagulation or condensation. The overall transition majorant rate is defined as [44]:

$$\hat{R}^{\mathrm{tr}} = \min(R^{\mathrm{sf}}, \hat{R}^{\mathrm{fm}}), \tag{11}$$

where the slip-free rate which does not require a majorant due to its simple form is:

$$R^{\mathrm{sf}} = \sum_{i \neq j}^{N(t)} K^{\mathrm{sf}}(P_q, P_r), \tag{12}$$

and the free-molecular majorant rate is [24]:

$$\hat{R}^{\mathrm{fm}} = \sum_{i \neq j}^{N(t)} \hat{K}^{\mathrm{fm}}(P_q, P_r). \tag{13}$$

In DSA, the number of stochastic particles is not conserved which leads to two problems: First, attempting to add a particle when the number of particles in the system has already reached the maximum possible number of particles. Second, removing particles until no particles remain. Inception, coagulation and condensation events remove particles because the particle ensemble includes both gas-phase PAHs (a stochastic particle composed of a single primary containing a single PAH) and particles (stochastic particles made up of two or more PAHs). A contraction algorithm is used to solve the first problem whereby, once the ensemble capacity is saturated, a particle is uniformly selected from the ensemble and discarded. The sample volume is then reduced by $N/(N+1)$. The second problem is corrected using a particle doubling algorithm [50]. Once the particle count falls below a doubling limit, N_{lim}, the particles are copied and the sample volume is doubled in order to allow the maintenance of a statistically significant number of particles in the system and avoid the eventual formation of a single large particle. The maximum number of stochastic particles in the system is N_{max} and the actual particle count lies in the range of $[N_{\mathrm{lim}}, N_{\mathrm{max}}]$ except during the initial transient when particles are inserted into the ensemble for the first time; the number of stochastic particles has to first exceed 75 % of N_{max} for the doubling algorithm to be activated. The doubling limit is defined in terms of the number of levels in the binary tree, l, that is used to store the ensemble of stochastic particles [24]:

$$N_{\mathrm{lim}} = \begin{cases} \dfrac{N_{\mathrm{max}}}{2} - 2^{l-5}, & l - 5 > 0, \\ \dfrac{N_{\mathrm{max}}}{2} - 2^{0}, & l - 5 \leq 0, \end{cases} \tag{14}$$

where $l = \log(N_{\max})/\log(2)$.

Through a combination of storing the exact structure of each PAH and the sheer number of PAHs that is modelled, the simulations that are performed require a large amount of memory. Assuming a soot density of 1.5 g cm^{-3} [5], and that a representative soot particle in a laminar co-flow ethylene diffusion flame has an average of 100 primary particles in point contact, each with an average diameter of 50 nm [45], we estimate that each soot particle is made up of about 5×10^8 carbon atoms. If we are to track the position of each carbon atom (an x and y integer coordinate is associated with each position), a single particle will have a memory usage of 2 GB. A typical simulation requires at least 128 stochastic particles which gives rise to a total memory usage of 256 GB.

We reduce the memory usage by reducing the number of carbon atoms (or PAHs) that are represented. Each time the ensemble is doubled, PAHs within a particle which is copied point to the same memory location as PAHs in the original particle. The advantage of such a strategy is that it significantly reduces the memory usage while retaining the ability to model the exact structure of each PAH. The same treatment cannot be applied to PAHs in the gas phase as the growth rate of a gas-phase PAH is different from the growth rate of a PAH which may have condensed onto a particle or has stuck onto another gas-phase PAH ($g \neq 1$ and $n_{\text{crit}} \geq 2$). Algorithm 1 describes DSA and the approximation that is introduced. Note that for implementation reasons we do not distinguish between a PAH in the gas phase and a PAH in a particle in the algorithm.

5 Results and discussion

5.1 Soot volume fraction

The soot volume fraction for the co-flow diffusion flame is measured using laser-induced incandescence (LII) [29] and laser extinction [1] for four different ethylene/nitrogen compositions (volume basis) of 32%/68%, 40%/60%, 60%/40% and 80%/20%. Figure 2 shows a comparison of soot volume fraction derived from LII (cross symbols) and extinction (circle symbols) measurements along the centerline of the 60%-C_2H_4/40%-N_2 flame. Despite calibrating LII signals against extinction measurements, the large difference in the results especially at medium heights is apparent. This might be due to experimental uncertainty. As discussed in detail by Santoro and Shaddix [54] uncertainties in the soot extinction coefficient can lead to an uncertainty on the order of a factor of 2 in the soot volume fraction. The experimental measurements in Fig. 2 fall within this experimental uncertainty.

Multiple experiments studying the influence of wavelength in extinction measurements have demonstrated that large PAHs may absorb light below wavelengths of about 700 nm [37, 68]. The extinction measurements in Fig. 2 are performed at a visible wavelength of 500 nm [1] which can possibly result in the higher extinction-derived soot volume fraction. We examine the sensitivity of the soot volume fraction to PAHs in the gas phase by computing the soot volume fraction based on gas-phase PAHs and particles (continuous line on Fig. 2) and particles alone (dash-dot-dashed line on Fig. 2). At low to

Input: State of the system Q_0 at initial time t_0; Final time t_f.
Output: State of the system Q_f at final time t_f.
$t_i \longleftarrow t_0$, $Q_i \longleftarrow Q_0$;
while $t_i < t_f$ **do**
Update particle ensemble to match the concentration profile of benzene that is supplied as input.

Calculate waiting time τ, with τ being exponentially distributed with rate $\hat{R}_{tr}(Q)$ given by Eq. (11).
Select two particles P_q and P_r according to the distribution:

$$\frac{K^{sf}(P_q,P_r)}{\hat{R}^{tr}(Q)} \text{ when } \hat{R}^{tr} = R^{sf} \text{ and } \frac{\hat{K}^{fm}(P_q,P_r)}{\hat{R}^{tr}(Q)} \text{ otherwise.}$$

Calculate:

$$\hat{K}(P_q,P_r) = K^{sf}(P_q,P_r) \text{ when } \hat{R}^{tr} = R^{sf} \text{ and } \hat{K}(P_q,P_r) = \hat{K}^{fm}(P_q,P_r) \text{ otherwise.}$$

Update deferred surface growth events for particles P_q and P_r.

With a probability $K^{tr}(P_q,P_r)/\hat{K}(P_q,P_r)$,
if $n_{PAHs}(P_q) == 1$ && $n_{PAHs}(P_r) == 1$ **then**
perform inception,
else if $n_{PAHs}(P_q) > 1$ && $n_{PAHs}(P_r) > 1$ **then**
perform coagulation,
else
perform condensation,
end
where $K^{tr}(P_q,P_r)$ is the transition kernel given in Eq. (9) and n_{PAHs} is the number of PAHs in the particle.

If necessary, perform particle doubling, so
if $N < N_{lim}$ **then**
for *each particle* $P \in \{P_1,\ldots,P_N\}$ **do**
if $n_{PAHs}(P) < n_{crit}$ **then**
Create a unique copy of the particle
else
Create a copy of the particle where PAHs in the copy point to the same memory location as PAHs in the original particle
end
end
end
Double sampling volume.

Update sintering level of all particles using Eq. (7).
Increment $t \longleftarrow t + \tau$.
end

Algorithm 1: Direct simulation algorithm with particle doubling.

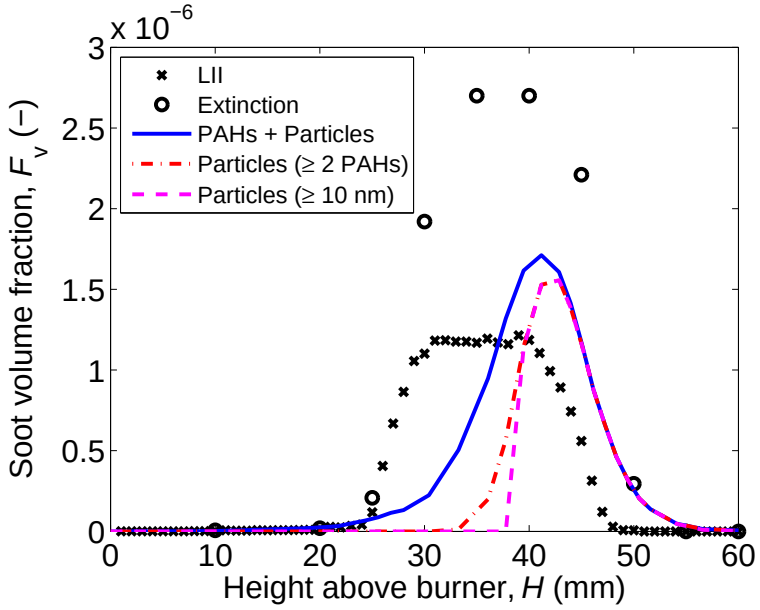

Figure 2: *Comparison of experimental (symbols) and computed (lines) centreline soot volume fraction for the 60%-C_2H_4/40%-N_2 flame. The soot volume fraction is computed for gas-phase PAHs and particles (continuous line), only particles made up of* ≥ 2 *PAHs (dash-dot-dashed line), and only particles with a collision diameter* ≥ 10 *nm (dashed line). Cross symbols represent soot volume fraction derived from LII measurements [29] while circle symbols represent soot volume fraction derived from line-of-sight extinction measurements at 500 nm [1].*

medium heights, gas-phase PAHs make a significant contribution to the total soot volume fraction as PAHs have to undergo a sufficient number of surface growth events for a successful inception event to occur. However, once particles are formed, they grow rapidly and because of this the soot volume fraction only displays a small sensitivity to the minimum size of particles - a dimer or larger vs a particle with a minimum collision diameter of 10 nm (dashed line on Fig. 2). Comparatively, soot volume fraction in the wings is not at all sensitive to the gas-phase PAHs as shown by the radial slices at various heights in Fig. 3. Hence, it appears that the discrepancy in the experimental measurements is not due to the absorption of PAHs at the visible wavelength that is used. We note, however, that these conclusions should be taken as preliminary due to the limited agreement between model and experiment.

Overall, the model is in qualitative agreement with the experiment and it is able to capture the experimentally observed transition of peak soot in the wings to the centerline with increasing height above burner. Quantitatively, however, the profiles differ notably. First, not only does the model underpredict soot along the centerline but there also appears to be a spatial discrepancy between the model and experiment. Second, the computed wings of the flame extend much beyond those determined by either experimental measurement. Considering that soot particles may diffuse from the wings of the flame to the centerline and that our model inherently neglects streamwise diffusion, it is important to understand the contribution of this process. The diffusion coefficient of soot with a density of

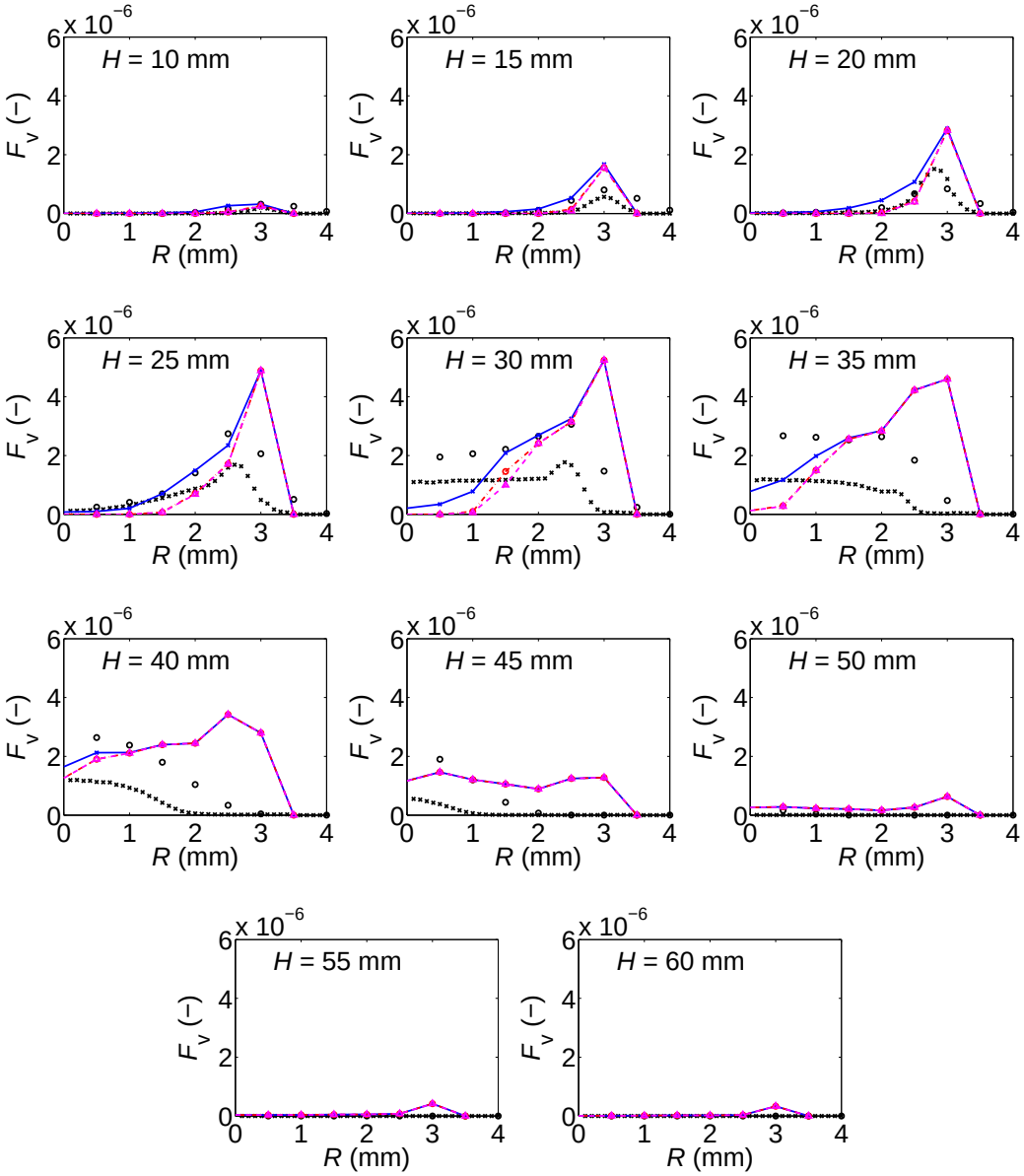

Figure 3: *Comparison of experimental (symbols) and computed (line through symbols) radial soot volume fraction at various heights of the 60%-C_2H_4/40%-N_2 flame. The soot volume fraction is computed for gas-phase PAHs and particles (continuous line), only particles made up of ≥ 2 PAHs (dash-dot-dashed line), and only particles with a collision diameter ≥ 10 nm (dashed line). Cross symbols represent soot volume fraction derived from LII measurements [29] while circle symbols represent soot volume fraction derived from line-of-sight extinction measurements at 500 nm [1]. F_v is the soot volume fraction, H is the height above the burner and R is the radial distance from the center of the burner.*

1.5 g cm^{-3} [5] is 9.2×10^{-44}, 1.0×10^{-42} and 4.1×10^{-42} m^2 s^{-1} for particle diameters of 3, 10 and 20 nm [15], respectively, at a flame temperature of 2000 K. Therefore, the

diffusion of soot will only have a negligible impact on the modelling results. A possible explanation for the spatial discrepancy on the centerline and the extended wings is considered below.

5.2 Optical band gap

OBG is determined as a function of axial and radial position from extinction data [1]. In this work we focus on the 60%-C_2H_4/40%-N_2 flame (the 80%-C_2H_4/20%-N_2 flame is qualitatively similar) as the amount of data and fidelity of the data in the 32%-C_2H_4/68%-N_2 and 40%-C_2H_4/60%-N_2 flames are limited. The experimental OBG can be correlated with the number of aromatic rings in a PAH [1] which can subsequently be compared with the model as shown by the continuous line in Fig. 4 along the centerline of the 60%-C_2H_4/40%-N_2 flame. The computed number of aromatic rings in a PAH is calculated as an average across all PAHs in the gas phase and in particles. Just above the burner the computed PAH size corresponds to benzene because no surface growth has taken place. While the model underpredicts the PAH size at low to medium heights, it is in relatively good agreement with the experimental data further downstream. This is to be expected since, computationally, the minimum number of aromatic rings in a PAH for a successful inception event to occur is chosen as 16. Overall, the simulations underpredict the PAH size along the centerline and overpredict the PAH size in the wings of the flame as shown by the radial slices at various heights (continuous lines) in Fig. 5. In what follows, we shall carry out sensitivity analysis on the most important model parameters to understand the plausible cause for the discrepancy.

5.3 Parametric sensitivity study

Sensitivity analyses are conducted by varying (a) the minimum number of aromatic rings in a PAH for inception (14–16 rings), (b) the growth factor (0.0263–0.1) and (c) the size of the smallest PAH which is assumed to contribute to the OBG (1–16 rings). The growth factor is not reduced below 0.0263 as it is the same factor that is applied to the oxidation rate of PAHs in particles. It has to be sufficiently large if particles are to be completely oxidised. The computations are carried out for the 60%-C_2H_4/40%-N_2 flame.

The minimum number of aromatic rings for inception of 16 rings is chosen to give a computed PAH size which best fits the experimental data; therefore, it is important to understand the sensitivity of the computed PAH size to this parameter. The minimum number of aromatic rings for inception is reduced from 16 to 14 rings, which results in at most a 3-ring decrease in the computed PAH size. The change in the computed PAH size is within the experimental uncertainty. Likewise, the growth factor is increased from 0.0263 to 0.1 and the computed PAH size along the centerline appears to be insensitive ($<$ 10 % increase) whereas it has a pronounced effect (percentage increase on the order of 10^2) in the wings. Temperature peaks at much lower heights above burner in the wings compared to the centerline; therefore, the surface growth rate is significantly higher in the wings. Overall, neither parameter displays the sensitivity to be able to reconcile the discrepancy between the experimental and computed PAH size.

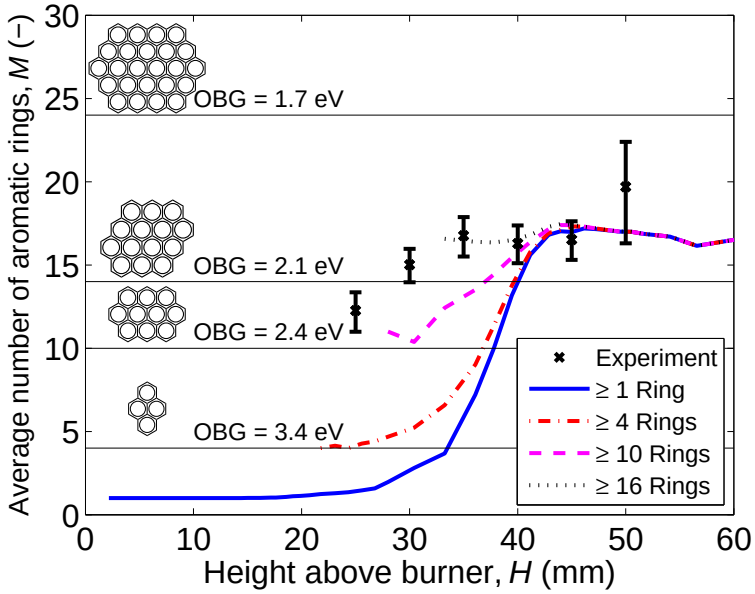

Figure 4: *Sensitivity, along the centerline, of the computed (lines) average number of aromatic rings in a PAH to the size of the smallest PAH which is assumed to contribute to the OBG for the 60%-C_2H_4/40%-N_2 flame. Symbols are experimental data. Representative PAH structures and the OBG associated with these structures are shown.*

Increasing the size of the smallest PAH which is assumed to contribute to the OBG leads to a systematic increase in the PAH size and a delay in the residence time at which PAHs contribute to the computed PAH size as shown in Figs. 4 and 5. The best results are obtained accounting for PAH contribution in both gas and particle phases assuming a minimum size of ovalene (10 rings). This suggests that the extinction measurements (from which the OBG is derived) show a significant absorption by PAHs in the gas phase at the visible wavelength that is used. This has been demonstrated by experiments in the literature [37, 68]. A summary of the influence of the model parameters on the soot volume fraction along the centerline and in the wings is shown in Fig. 6.

6 Implications on underlying simulations

The underlying predictions of certain key gas-phase species [29] differ quite significantly from the experimental data that is available for the 60%-C_2H_4/40%-N_2 flame [58]. Therefore, we would like to investigate the dependence of the post-processed results on the underlying gas-phase profiles. The soot volume fraction contour derived from LII measurements and the computed contour, both taken from Herdman et al. [29], are shown in the left and middle panels, respectively, of Fig. 7. Two principal deficiencies in the soot model [58] are observed: (a) not only does the model substantially underpredicts soot on the centerline, but also yields the onset of particle nucleation later than the experimental counterpart; (b) the model predicts that the length of the wings as indicated by the peak

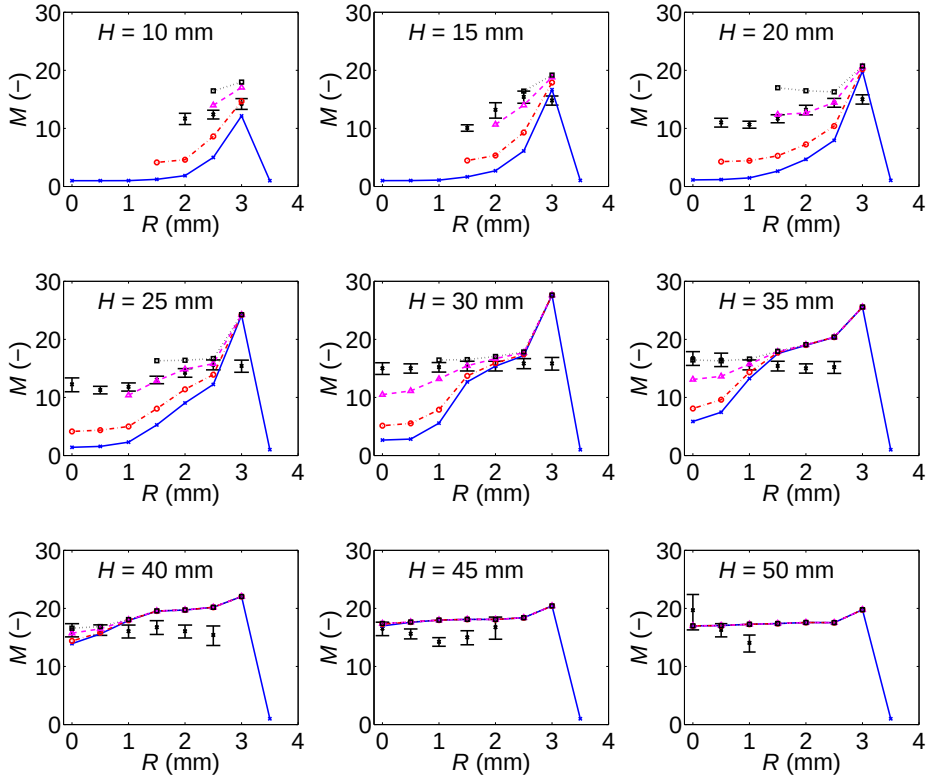

Figure 5: *Sensitivity, in the radial direction, of the computed (line through symbols) average number of aromatic rings in a PAH to the size of the smallest PAHs which is assumed to contribute to the OBG (continuous line: $\geq$ 1 Ring; dash-dot-dashed line: $\geq$ 4 Rings; dashed line: $\geq$ 10 Rings; dotted line: $\geq$ 16 Rings) at various heights of the 60%-C_2H_4/40%-N_2 flame. Symbols are experimental data. M is the number of aromatic rings in a PAH, H is the height above the burner and R is the radial distance from the center of the burner.*

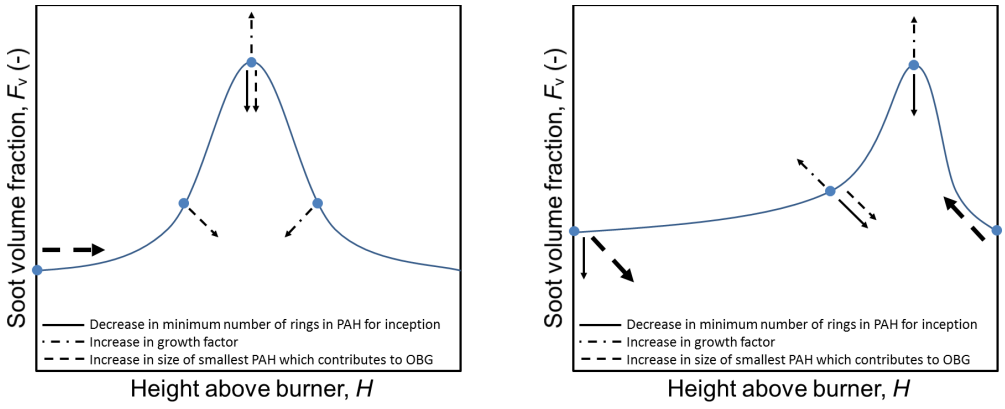

Figure 6: *Summary of effects of key model parameters on the soot volume fraction along the centerline (left panel) and in the wings (right panel).*

soot volume fraction overextends beyond the experiment. We find the same problems in the simulations we perform as a postprocessing step.

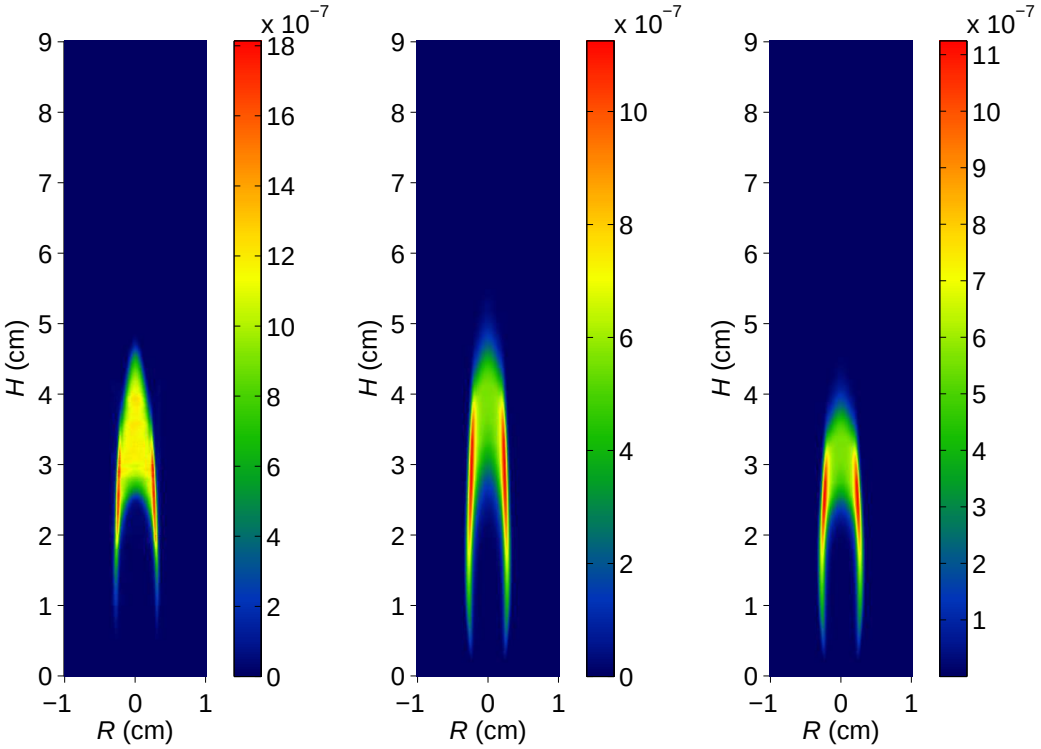

Figure 7: *Comparison of the soot volume fraction contour derived from LII measurements (left panel) with the computed soot volume fraction contours (middle and right panels) for the 60%-C_2H_4/40%-N_2 flame. In the middle panel the length of the computational domain is left unchanged while in the right panel it is scaled by the function shown in Fig. 8. Both experimental and computed results are taken from Herdman et al. [29]. H is the height above the burner and R is the radial distance from the center of the burner.*

To investigate the relationship between the underlying gas-phase profiles provided as input to the detailed soot model and the properties of soot predicted by the model, we apply a scaling factor f to the length of the profiles while leaving the magnitudes of the temperature and species concentrations unchanged:

$$f(H) = \begin{cases} 1.0, & H \leq 1.43 \text{ cm}, \\ 0.0402H^3 - 0.2976H^2 + 0.6052H + 0.6256, & 1.43 < H \leq 3.5 \text{ cm}, \\ 0.8217, & H > 3.5 \text{ cm}. \end{cases} \quad (15)$$

The scaling factor we have chosen is an attempt to reproduce the experimental soot volume fraction contour. The computed contour after scaling is shown in the right panel of Fig. 7. The scaling factor is shown in Fig. 8.

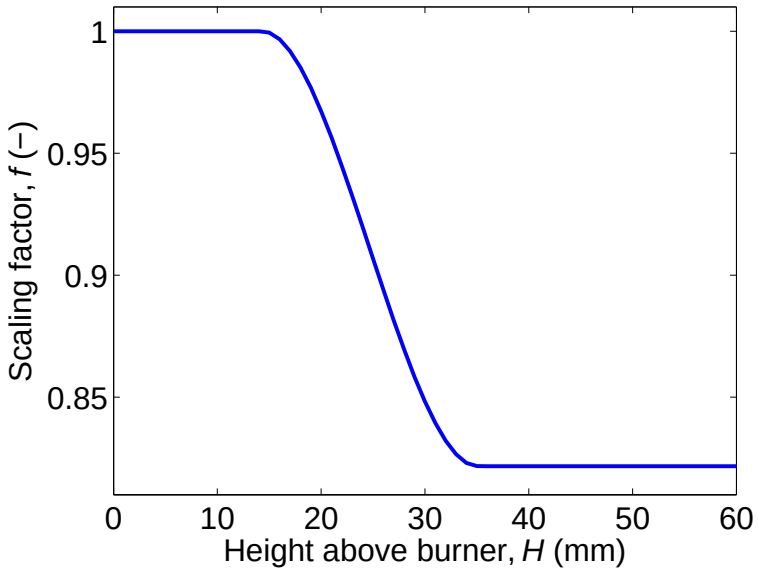

Figure 8: *Scaling factor as a function of height above burner.*

The computed temperature and acetylene profiles after scaling are in better agreement with the experiment as shown in Fig. 9; however, a discrepancy remains in the benzene profile. To ascertain the influence of this discrepancy on the model results, we impose the experimental temperature, benzene and acetylene gas-phase profiles. Fig. 10 shows a comparison of the computed soot volume fraction along the centerline where the energy equation and related species equations are solved (dash-dot-dashed line) and where the experimental profiles are imposed (dashed line). Imposing the experimental profiles, in fact, results in a decrease in the soot volume fraction which shows that the remaining difference between model and experiment cannot be attributed to uncertainties in the PAH chemistry. Overall, the computed soot volume fraction and OBG after scaling are in better agreement with the experiment (Figs. 10 to 13). Hence, qualitatively and quantitatively accurate predictions of the temperature and main species concentrations are required to be able to accurately model soot using the postprocessing technique.

Despite the different soot particle histories and residence times in the flame, it is initially surprising that the PAH size as indicated by the OBG is similar throughout the flame. However the same behaviour is captured by our model. Figure 14(a) shows computed PAH size distributions along the centerline and the streamline with the highest soot volume fraction (the wings) at various heights along the flame. The average number of aromatic rings associated with the mode of the distributions and the maximum probability density of each of these distributions are shown in Figs. 14(b) and 14(c), respectively. Just above the burner, at a height of 5 mm, both PAH size distributions along the centerline and in the wings are unimodal with a mode at benzene. The PAH size distribution in the wings transitions through a bimodal distribution as flame temperatures are reached at a height of about 10 mm, thus enabling PAHs in the gas phase to grow large enough to form particles. From a height of 10 mm to 30 mm, the variance of the distribution increases as PAHs in particles continue to grow, albeit at a reduced rate ($g = 0.0263$), and from a height of 30 mm to 40 mm, the variance decreases as these PAHs are oxidised; however,

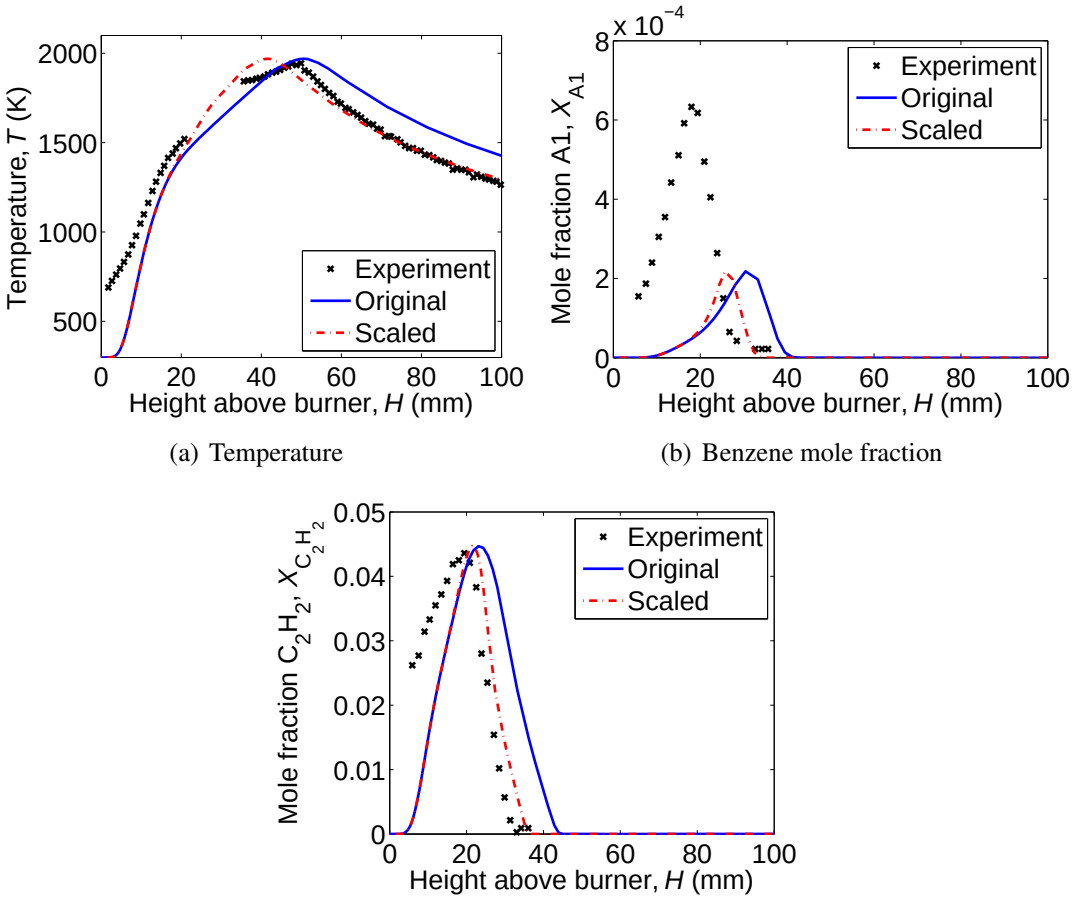

(a) Temperature

(b) Benzene mole fraction

(c) Acetylene mole fraction

Figure 9: *Comparison of experimental (symbols) and computed (lines) centreline temperature, benzene mole fraction, and acetylene mole fraction for the 60%-C_2H_4/40%-N_2 flame. Continuous line: the length of the profile is left unchanged; dash-dot-dashed line: the length of the profile is scaled by the function shown in Fig. 8.*

the PAH size associated with the mode remains about constant as shown in Fig. 14(b). Along the centerline, surface growth is much slower than in the wings as the temperature peaks at much larger heights above burner as compared with in the wings. PAHs only grow large enough to form particles at a height of about 30 mm. However, for heights thereafter, the PAH size associated with the mode of both distributions are similar which is consistent with the near-constant OBG that is observed experimentally.

7 Conclusions

We present a modelling study of soot formation for a laminar co-flow ethylene diffusion flame. A detailed population balance model is used to perform a parametric sensitivity

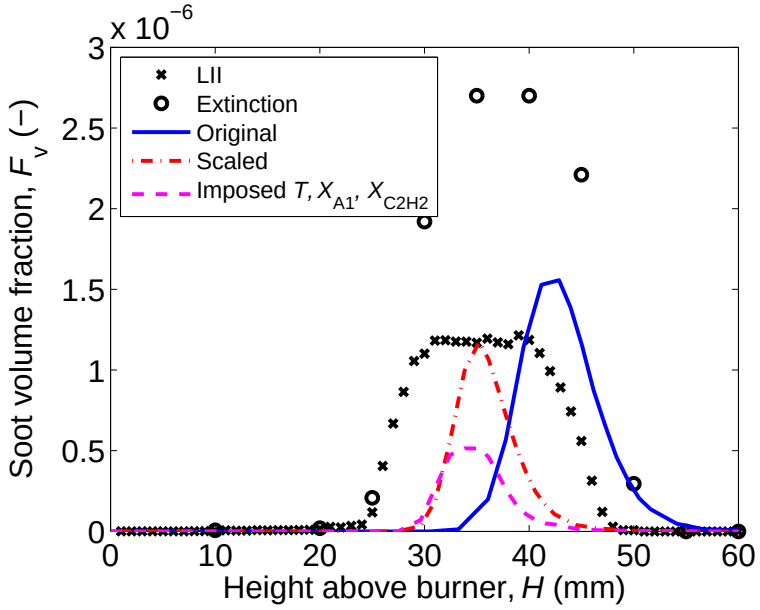

Figure 10: *Comparison of experimental (symbols) and computed centreline soot volume fraction where the length of the gas-phase profiles are left unchanged (continuous line), where the length of the profiles are scaled by the function shown in Fig. 8 (dash-dot-dashed line), and where the experimental temperature, benzene and acetylene profiles are imposed, all for the 60%-C_2H_4/40%-N_2 flame. The soot volume fraction is calculated for all particles made up of $\geq$ 2 PAHs. Cross symbols represent soot volume fraction derived from LII measurements [29] while circle symbols represent soot volume fraction derived from line-of-sight extinction measurements at 500 nm [1].*

study to understand the influence of the most important parameters on the computed OBG. We provide insight into soot formation using computed PAH size distributions along the centerline and in the wings of the flame.

We propose two zig-zag oxidation jump processes which allow PAHs to be completely oxidised. We set out a new stochastic algorithm for solving the population balance equations for soot particles in a laminar co-flow diffusion flame. The algorithm is found to offer significant reductions in memory usage.

The computed soot volume fraction captures the trend in the experimental data, with the transition of peak soot in the wings to the centerline with increasing height above burner. Including PAHs from the gas phase for the calculation of the soot volume fraction leads to a small, but notable, increase in the computed soot volume fraction along the centerline but has no significant effect in the wings of the flame. This suggests that the higher (as compared to LII) extinction-derived soot volume fractions are not due to absorption by PAHs at the visible wavelength that is used.

The base case simulations underpredict the PAH size along the centerline and overpredict the PAH size in the wings of the flame. A parametric sensitivity study is performed to understand the cause of the discrepancies between the experimental and computed OBG.

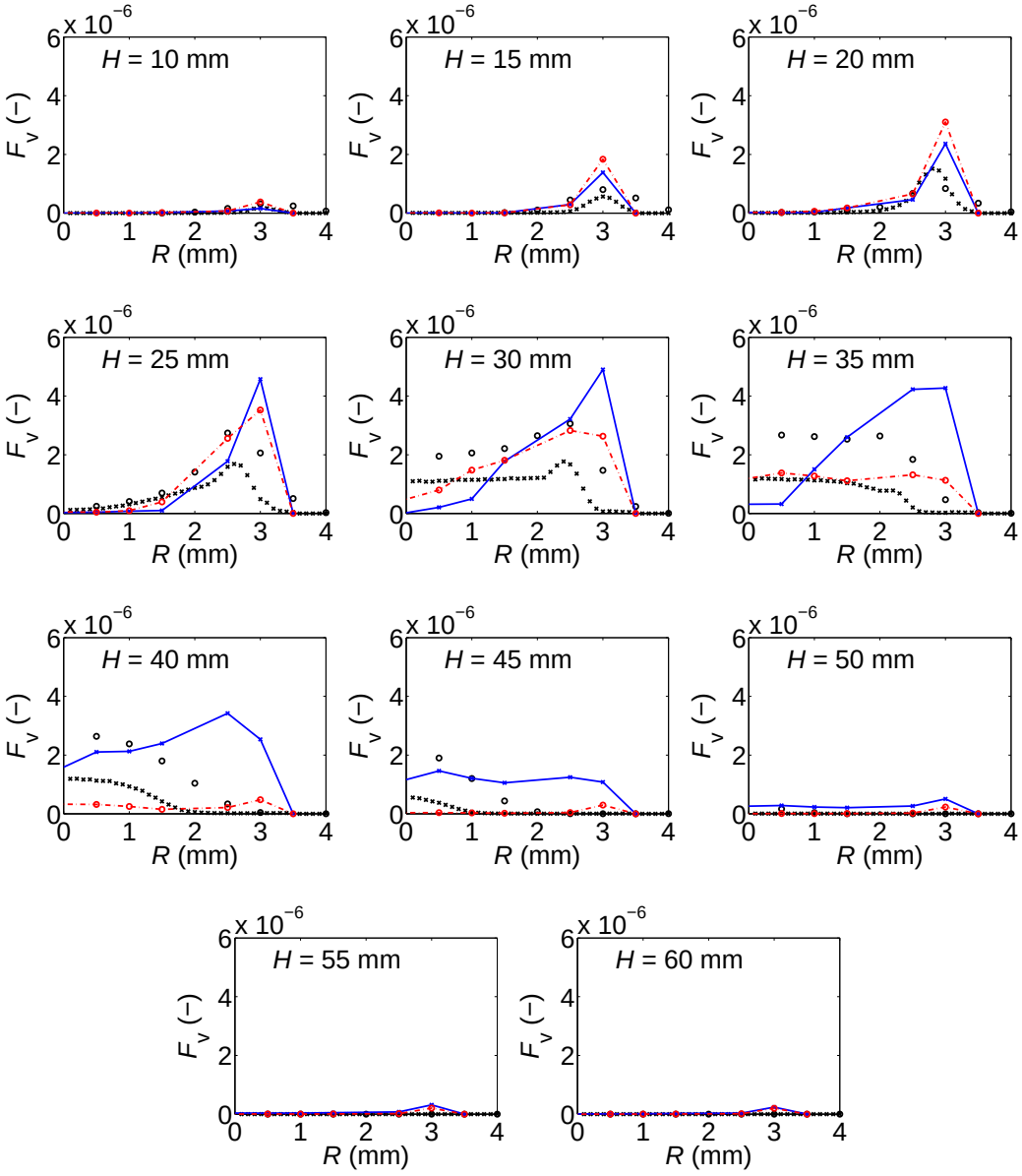

Figure 11: *Comparison of experimental (symbols) and computed (line through symbols) radial soot volume fraction at various heights of the 60%-C_2H_4/40%-N_2 flame. Continuous line: the length of the gas-phase profiles are left unchanged; dash-dot-dashed line: the length of the profiles are scaled by the function shown in Fig. 8. The soot volume fraction is calculated for all particles made up of $\geq$ 2 PAHs. Cross symbols represent soot volume fraction derived from LII measurements [29] while circle symbols represent soot volume fraction derived from line-of-sight extinction measurements at 500 nm [1]. F_v is the number of aromatic rings in a PAH, H is the height above the burner and R is the radial distance from the center of the burner.*

We find that the computed OBG is most sensitive to the size of the smallest PAH which

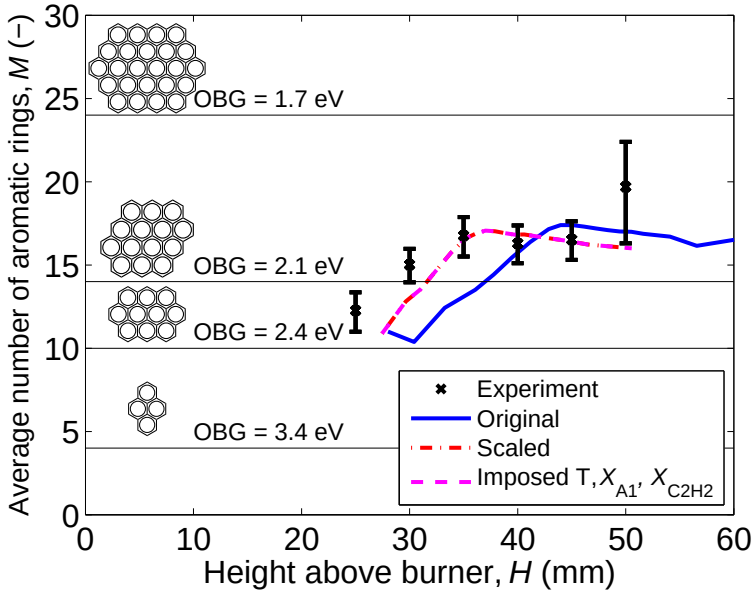

Figure 12: *Comparison of experimental (symbols) and computed average number of aromatic rings in a PAH where the length of the gas-phase profiles are left unchanged (continuous line), where the length of the profiles are scaled by the function shown in Fig. 8 (dash-dot-dashed line), and where the experimental temperature, benzene and acetylene profiles are imposed, all along the centerline of the 60%-C_2H_4/40%-N_2 flame. PAHs with at least 10 aromatic rings are assumed to contribute to the OBG.*

is assumed to contribute to the OBG. The best results are obtained accounting for PAH contribution in both gas and particle phases assuming a minimum size of ovalene (10 rings). This suggests that the extinction measurements (from which the OBG is derived) show a significant absorption by PAHs in the gas phase at the visible wavelength that is used, which has been demonstrated by experiments in the literature. A scaling factor is applied to the length of the underlying gas-phase profiles which goes some way towards explaining the discrepancy between the experiment and model. In particular, the onset of nucleation along the centerline occurs earlier and the extended wings are eliminated, thus bringing the modelling and experimental results closer to each other. It is shown that PAH size distributions along the centerline and in the wings are unimodal at larger heights above burner. Despite the different soot particle histories and residence times in the flame, the PAH size associated with both modes are similar which is consistent with the near-constant OBG that is observed experimentally. The results of this study suggests that the critical PAH size for particle inception is about 16 aromatic rings which is consistent with recent experimental studies.

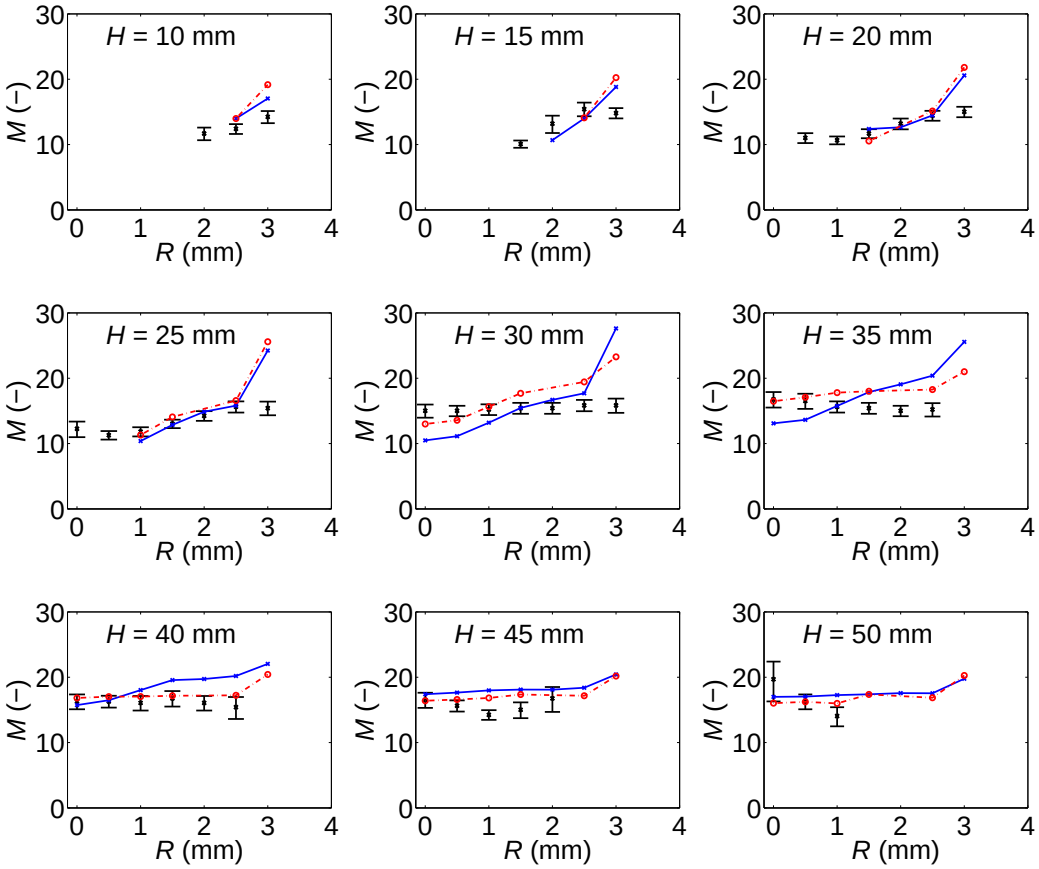

Figure 13: *Radial slices of experimental (symbols) and computed average number of aromatic rings in a PAH where the length of the gas-phase profiles are left unchanged (continuous line) and where the length of the profiles are scaled by the function shown in Fig. 8 (dash-dot-dashed line), both for the 60%-C_2H_4/40%-N_2 flame. PAHs with at least 10 aromatic rings are assumed to contribute to the OBG. M is the number of aromatic rings in a PAH, H is the height above the burner and R is the radial distance from the center of the burner.*

Acknowledgements

Financial support by the Gates Cambridge is gratefully acknowledged. This project is partly funded by the National Research Foundation (NRF), Prime Minister's Office, Singapore under its Campus for Research Excellence and Technological Enterprise (CREATE) programme. Professor Markus Kraft has been supported by the Weierstrass Institute for Applied Analysis and Stochastics.

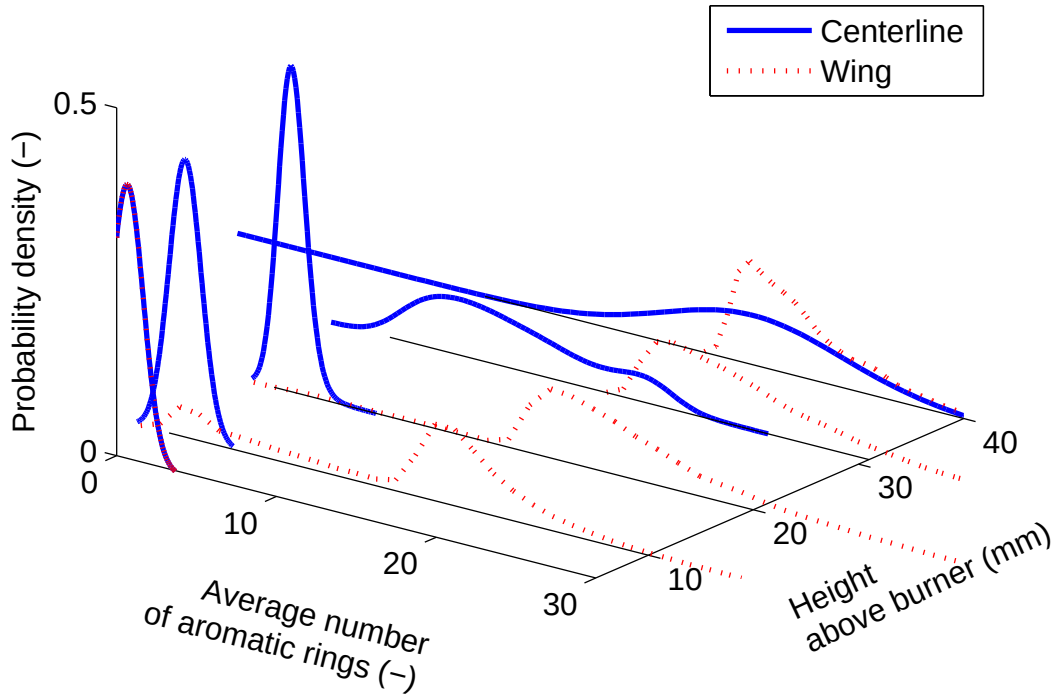

(a) Comparison of computed PAH size distributions along the centerline (continuous line) and along the streamline with the highest soot volume fraction (dotted line) at various heights of the 60%-C_2H_4/40%-N_2 flame. For both streamlines the length of the computational domain are scaled by the function in Fig. 8.

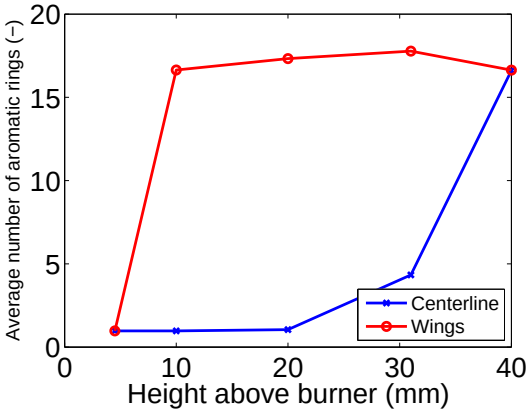

(b) The average number of aromatic rings associated with the mode of the distributions in Fig. 14(a) along the centerline and in the wings

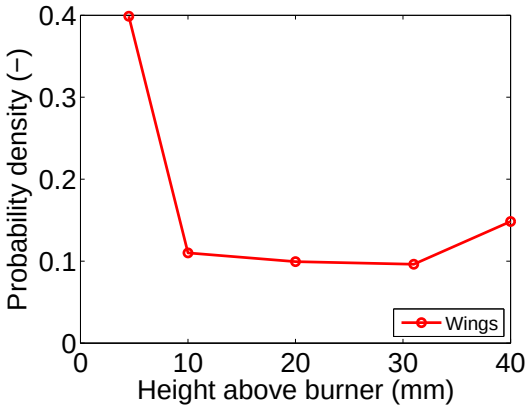

(c) The maximum probability density of each of the distributions in Fig. 14(a) along the wings

Figure 14: *Evolution of computed PAH size distributions throughout the flame.*

Nomenclature

Greek

α	Absorption coefficient (m^{-1}), see Eq. (1)
ρ	Density ($kg\,m^{-3}$), see Eq. (7)
τ	Exponentially distributed waiting time (s)
τ_s	Sintering time (s), see Eq. (6)

Mathematical notations

$\hat{x}$	Majorant ($m^{-3}\,s^{-1}$), see Eq. (10)

Lower-case Roman

c	Sintering level (-), see Eq. (7)
$d_{i,j}$	Minimum diameter of neighbouring primary particles p_i and p_j (m), see Eq. (6)
d_{crit}	Critical primary particle diameter below which primaries are assumed to be liquid-like and sinter instantaneously (m), see Eq. (6)
f	Scaling factor (-), see Eq. (15)
g	Growth factor (-)
hv	Photon energy (eV), see Eq. (1)
l	Number of levels in binary tree (-), see Eq. (14)
n_{crit}	Critical number of PAHs in primary particle before growth factor is applied (-)
n_{PAHs}	Number of PAHs in particle (-)
r	Tauc exponent which determines the type of transition (-), see Eq. (1)
s	Smoothing factor (-)
t	Time (s), see Eq. (5)

Subscripts

C_2H_2	Acetylene
A1	Benzene
crit	Critical, see Eq. (4)
f	Final
g	Gap, see Eq. (1)
i	Index of time interval
i, j	Index of primary particles, see Eq. (5)
lim	Limit, see Eq. (14)
max	Maximum, see Eq. (14)
N	Number of stochastic particles (-)
PAHs	Polycyclic aromatic hydrocarbons, see Eq. (4)
q, r	Index of particle, see Eq. (8)
s	Sintering, see Eq. (6)
v	Volume
0	Initial

Upper-case Roman

A Pre-exponential factor ($\mathrm{s\,m^{-1}}$), see Eq. (6)
C Common surface area between two primary particles ($\mathrm{m^2}$), see Eq. (5)
E Activation energy (K), see Eq. (6)
E_g Optical band gap (eV), see Eq. (1)
F_v Soot volume fraction (-)
H Height above burner (m), see Eq. (15)
K Kernel ($\mathrm{m^{-3}\,s^{-1}}$), see Eq. (8)
M Number of 6-member aromatic rings in PAH (-), see Eq. (2)
N Number of stochastic particles (-), see Eq. (8)
P Particle (-), see Eq. (8)
Q State of system
R Radial distance from centerline of burner (m)
R Rate ($\mathrm{m^{-3}\,s^{-1}}$), see Eq. (8)
S Surface area of a sphere ($\mathrm{m^2}$), see Eq. (5)
T Temperature (K), see Eq. (6)
X Mole fraction (-)

Superscripts

fm Free-molecular, see Eq. (9)
sf Slip-flow, see Eq. (9)
tr Transition, see Eq. (9)

References

[1] E. M. Adkins and J. H. Miller. Extinction measurements for optical band gap determination of soot in a series of nitrogen-diluted ethylene/air non-premixed flames. *Phys. Chem. Chem. Phys.*, 17:2686–2695, 2015. doi:10.1039/C4CP04452E.

[2] J. Akroyd, A. J. Smith, R. Shirley, L. R. McGlashan, and M. Kraft. A coupled CFD-population balance approach for nanoparticle synthesis in turbulent reacting flows. *Chem. Eng. Sci.*, 66:3792–3805, 2011. doi:10.1016/j.ces.2011.05.006.

[3] B. Apicella, P. Pré, M. Alfè, A. Ciajolo, V. Gargiulo, C. Russo, A. Tregrossi, D. Deldique, and J. N. Rouzaud. Soot nanostructure evolution in premixed flames by High Resolution Electron Transmission Microscopy (HRTEM). *Proc. Combust. Inst.*, 35:1895–1902, 2015. doi:10.1016/j.proci.2014.06.121.

[4] M. Balthasar and M. Kraft. A stochastic approach to calculate the particle size distribution function of soot particles in laminar premixed flames. *Combust. Flame*, 133:289–298, 2003. doi:10.1016/S0010-2180(03)00003-8.

[5] J. Camacho, C. Liu, C. Gu, H. Lin, Z. Huang, Q. Tang, X. You, C. Saggese, Y. Li, H. Jung, L. Deng, I. Wlokas, and H. Wang. Mobility size and mass of nascent soot particles in a benchmark premixed ethylene flame. *Combust. Flame*, 2015. doi:10.1016/j.combustflame.2015.07.018.

[6] M. Celnik, A. Raj, R. West, R. Patterson, and M. Kraft. Aromatic site description of soot particles. *Combust. Flame*, 155:161–180, 2008. doi:10.1016/j.combustflame.2008.04.011.

[7] M. S. Celnik, M. Sander, A. Raj, R. H. West, and M. Kraft. Modelling soot formation in a premixed flame using an aromatic-site soot model and an improved oxidation rate. *Proc. Combust. Inst.*, 32:639–646, 2009. doi:10.1016/j.proci.2008.06.062.

[8] D. Chen, Z. Zainuddin, E. Yapp, J. Akroyd, S. Mosbach, and M. Kraft. A fully coupled simulation of PAH and soot growth with a population balance model. *Proc. Combust. Inst.*, 34:1827–1835, 2013. doi:10.1016/j.proci.2012.06.089.

[9] H. Chen and R. Dobbins. Crystallogenesis of particles formed in hydrocarbon combustion. *Combust. Sci. Technol.*, 159:109–128, 2000. doi:10.1080/00102200008935779.

[10] M. Commodo, G. Tessitore, G. De Falco, A. Bruno, P. Minutolo, and A. D'Anna. Further details on particle inception and growth in premixed flames. *Proc. Combust. Inst.*, 35:1795–1802, 2015. doi:10.1016/j.proci.2014.06.004.

[11] R. A. Dobbins, R. A. Fletcher, and H.-C. Chang. The evolution of soot precursor particles in a diffusion flame. *Combust. Flame*, 115:285–298, 1998. doi:10.1016/S0010-2180(98)00010-8.

[12] S. B. Dworkin, M. D. Smooke, and V. Giovangigli. The impact of detailed multicomponent transport and thermal diffusion effects on soot formation in ethylene/air flames. *Proc. Combust. Inst.*, 32:1165–1172, 2009. doi:10.1016/j.proci.2008.05.061.

[13] A. Eibeck and W. Wagner. An efficient stochastic algorithm for studying coagulation dynamics and gelation phenomena. *SIAM J. Sci. Comput.*, 22:802–821, 2000. doi:10.1137/S1064827599353488.

[14] A. Eibeck and W. Wagner. Approximative solution of the coagulation–fragmentation equation by stochastic particle systems. *Stoch. Anal. Appl.*, 18:921–948, 2000. doi:10.1080/07362990008809704.

[15] P. S. Epstein. On the resistance experienced by spheres in their motion through gases. *Phys. Rev.*, 23:710–733, 1924. doi:10.1103/PhysRev.23.710.

[16] M. Frenklach. On surface growth mechanism of soot particles. *Proc. Combust. Inst.*, 26:2285–2293, 1996. doi:10.1016/S0082-0784(96)80056-7.

[17] M. Frenklach. Reaction mechanism of soot formation in flames. *Phys. Chem. Chem. Phys.*, 4:2028–2037, 2002. doi:10.1039/b110045a.

[18] M. Frenklach and H. Wang. Detailed modeling of soot particle nucleation and growth. *Proc. Combust. Inst.*, 23:1559–1566, 1990. doi:10.1016/S0082-0784(06)80426-1.

[19] M. Frenklach and H. Wang. Detailed surface and gas-phase chemical kinetics of diamond deposition. *Phys. Rev. B*, 43:1520–1545, 1991. doi:10.1103/PhysRevB.43.1520.

[20] M. Frenklach, D. W. Clary, W. C. Gardiner Jr., and S. E. Stein. Detailed kinetic modeling of soot formation in shock-tube pyrolysis of acetylene. *Proc. Combust. Inst.*, 20:887–901, 1984. doi:10.1016/S0082-0784(85)80578-6.

[21] S. K. Friedlander. *Smoke, dust, and haze*. Wiley, New York, 1977.

[22] N. A. Fuchs. *The mechanics of aerosols*. Pergamon, Oxford, 1964.

[23] F. Gelbard and J. H. Seinfeld. Simulation of multicomponent aerosol dynamics. *J. Colloid Interface Sci.*, 78:485–501, 1980. doi:10.1016/0021-9797(80)90587-1.

[24] M. Goodson and M. Kraft. An efficient stochastic algorithm for simulating nano-particle dynamics. *J. Comput. Phys.*, 183:210–232, 2002. doi:10.1006/jcph.2002.7192.

[25] J. Happold. *Geschichtete polyzyklische aromatische Kohlenwasserstoffe als Bausteine der Rußbildung*. PhD thesis, Universität Stuttgart, Stuttgart, 2008.

[26] J. Happold, H.-H. Grotheer, and M. Aigner. Distinction of gaseous soot precursor molecules and soot precursor particles through photoionization mass spectrometry. *Rapid Commun. Mass Spectrom.*, 21:1247–1254, 2007. doi:10.1002/rcm.2955.

[27] J. Happold, H.-H. Grotheer, and M. Aigner. Soot precursors consisting of stacked pericondensed PAHs. In H. Bockhorn, A. D'Anna, A. F. Sarofim, H. Wang (Eds.), *Combustion generated fine carbonaceous particles* (pp. (277–288)). KIT Scientific Publishing: Karlsruhe, 2009.

[28] B. S. Haynes and H. Gg. Wagner. Soot formation. *Prog. Energy Combust. Sci.*, 7: 229–273, 1981. doi:10.1016/0360-1285(81)90001-0.

[29] J. D. Herdman, B. C. Connelly, M. D. Smooke, M. B. Long, and J. H. Miller. A comparison of Raman signatures and laser-induced incandescence with direct numerical simulation of soot growth in non-premixed ethylene/air flames. *Carbon*, 49: 5298–5311, 2011. doi:10.1016/j.carbon.2011.07.050.

[30] K. H. Homann. Formation of large molecules, particulates and ions in premixed hydrocarbon flames; progress and unresolved questions. *Proc. Combust. Inst.*, 20: 857–870, 1985. doi:10.1016/S0082-0784(85)80575-0.

[31] J. B. Howard. Carbon addition and oxidation reactions in heterogeneous combustion and soot formation. *Proc. Combust. Inst.*, 23:1107–1127, 1991. doi:10.1016/S0082-0784(06)80371-1.

[32] I. C. Jaramillo, C. K. Gaddam, R. L. Vander Wal, and J. S. Lighty. Effect of nanostructure, oxidative pressure and extent of oxidation on model carbon reactivity. *Combust. Flame*, 162:1848–1856, 2015. doi:10.1016/j.combustflame.2014.12.006.

[33] Ü. Ö. Köylü, C. S. McEnally, D. E. Rosner, and L. D. Pfefferle. Simultaneous measurements of soot volume fraction and particle size / microstructure in flames using a thermophoretic sampling technique. *Combust. Flame*, 110:494–507, 1997. doi:10.1016/S0010-2180(97)00089-8.

[34] P. Lavvas, M. Sander, M. Kraft, and H. Imanaka. Surface chemistry and particle shape: processes for the evolution of aerosols in Titan's atmosphere. *Astrophys. J.*, 728:80, 2011. doi:10.1088/0004-637X/728/2/80.

[35] C. S. McEnally, A. M. Schaffer, M. Long, L. D. Pfefferle, M. D. Smooke, M. B. Colket, and R. J. Hall. Computational and experimental study of soot formation in a coflow, laminar ethylene diffusion flame. *Proc. Combust. Inst.*, 27:1497–1505, 1998. doi:10.1016/S0082-0784(98)80557-2.

[36] W. J. Menz and M. Kraft. A new model for silicon nanoparticle synthesis. *Combust. Flame*, 160:947–958, 2013. doi:10.1016/j.combustflame.2013.01.014.

[37] F. Migliorini, K. A. Thomson, and G. J. Smallwood. Investigation of optical properties of aging soot. *Appl. Phys. B*, 104:273–283, 2011. doi:10.1007/s00340-011-4396-4.

[38] J. H. Miller. Aromatic excimers: evidence for polynuclear aromatic hydrocarbon condensation in flames. *Proc. Combust. Inst.*, 30:1381–1388, 2005. doi:10.1016/j.proci.2004.08.192.

[39] J. H. Miller, J. D. Herdman, C. D. O. Green, and E. M. Webster. Experimental and computational determinations of optical band gaps for PAH and soot in a N_2-diluted, ethylene/air non-premixed flame. *Proc. Combust. Inst.*, 34:3669–3675, 2013. doi:10.1016/j.proci.2012.05.054.

[40] N. Morgan, M. Kraft, M. Balthasar, D. Wong, M. Frenklach, and P. Mitchell. Numerical simulations of soot aggregation in premixed laminar flames. *Proc. Combust. Inst.*, 31:693–700, 2007. doi:10.1016/j.proci.2006.08.021.

[41] S. Mosbach, M. S. Celnik, A. Raj, M. Kraft, H. R. Zhang, S. Kubo, and K.-O. Kim. Towards a detailed soot model for internal combustion engines. *Combust. Flame*, 156:1156–1165, 2009. doi:10.1016/j.combustflame.2009.01.003.

[42] K. Ono, Y. Matsukawa, K. Dewa, A. Watanabe, K. Takahashi, Y. Saito, Y. Matsushita, H. Aoki, K. Era, T. Aoki, and T. Yamaguchi. Formation mechanisms of soot from high-molecular-weight polycyclic aromatic hydrocarbons. *Combust. Flame*, 162:2670–2678, 2015. doi:10.1016/j.combustflame.2015.03.022.

[43] R. I. A. Patterson, J. Singh, M. Balthasar, M. Kraft, and J. R. Norris. The Linear Process Deferment Algorithm: a new technique for solving population balance equations. *SIAM J. Sci. Comput.*, 28:303–320, 2006. doi:10.1137/040618953.

[44] R. I. A. Patterson, J. Singh, M. Balthasar, M. Kraft, and W. Wagner. Extending stochastic soot simulation to higher pressures. *Combust. Flame*, 145:638–642, 2006. doi:10.1016/j.combustflame.2006.02.005.

[45] R. Puri, T. F. Richardson, R. J. Santoro, and R. A. Dobbins. Aerosol dynamic processes of soot aggregates in a laminar ethene diffusion flame. *Combust. Flame*, 92: 320–333, 1993. doi:10.1016/0010-2180(93)90043-3.

[46] R. Puri, R. J. Santoro, and K. C. Smyth. The oxidation of soot and carbon monoxide in hydrocarbon diffusion flames. *Combust. Flame*, 97:125–144, 1994. doi:10.1016/0010-2180(94)90001-9.

[47] A. Raj, M. Celnik, R. Shirley, M. Sander, R. Patterson, R. West, and M. Kraft. A statistical approach to develop a detailed soot growth model using PAH characteristics. *Combust. Flame*, 156:896–913, 2009. doi:10.1016/j.combustflame.2009.01.005.

[48] A. Raj, M. Sander, V. Janardhanan, and M. Kraft. A study on the coagulation of polycyclic aromatic hydrocarbon clusters to determine their collision efficiency. *Combust. Flame*, 157:523–534, 2010. doi:10.1016/j.combustflame.2009.10.003.

[49] J. Robertson and E. P. O'Reilly. Electronic and atomic structure of amorphous carbon. *Phys. Rev. B*, 35:2946–2957, 1987. doi:10.1103/PhysRevB.35.2946.

[50] K. K. Sabelfeld, S. V. Rogasinsky, A. A. Kolodko, and A. I. Levykin. Stochastic algorithms for solving Smolouchovsky coagulation equation and applications to aerosol growth simulation. *Monte Carlo Methods Appl.*, 2:43–87, 1996. doi:10.1515/mcma.1996.2.1.41.

[51] M. Sander, A. Raj, O. Inderwildi, M. Kraft, S. Kureti, and H. Bockhorn. The simultaneous reduction of nitric oxide and soot in emissions from diesel engines. *Carbon*, 47:866–875, 2009. doi:10.1016/j.carbon.2008.11.043.

[52] M. Sander, R. H. West, M. S. Celnik, and M. Kraft. A detailed model for the sintering of polydispersed nanoparticle agglomerates. *Aerosol Sci. Technol.*, 43:978–989, 2009. doi:10.1080/02786820903092416.

[53] M. Sander, R. I. A. Patterson, A. Braumann, A. Raj, and M. Kraft. Developing the PAH-PP soot particle model using process informatics and uncertainty propagation. *Proc. Combust. Inst.*, 33:675–683, 2011. doi:10.1016/j.proci.2010.06.156.

[54] R. J. Santoro and C. R. Shaddix. Laser-induced incandescence. In K. Kohse–Höinghaus, J. B. Jeffries (Eds.), *Applied combustion diagnostics* (pp. (252–286)). Taylor & Francis: New York, 2002.

[55] M. Schenk, S. Lieb, H. Vieker, A. Beyer, A. Gölzhäuser, H. Wang, and K. Kohse-Höinghaus. Imaging nanocarbon materials: soot particles in flames are not structurally homogeneous. *ChemPhysChem*, 14:3248–3254, 2013. doi:10.1002/cphc.201300581.

[56] J. H. Seinfeld and S. N. Pandis. *Atmospheric chemistry and physics–from air pollution to climate change*. Wiley, New York, 1998.

[57] M. D. Smooke, C. S. McEnally, L. D. Pfefferle, R. J. Hall, and M. B. Colket. Computational and experimental study of soot formation in a coflow, laminar diffusion flame. *Combust. Flame*, 117:117–139, 1999. doi:10.1016/S0010-2180(98)00096-0.

[58] M. D. Smooke, R. J. Hall, M. B. Colket, J. Fielding, M. B. Long, C. S. McEnally, and L. D. Pfefferle. Investigation of the transition from lightly sooting towards heavily sooting co-flow ethylene diffusion flames. *Combust. Theor. Model.*, 8:593–606, 2004. doi:10.1088/1364-7830/8/3/009.

[59] M. D. Smooke, M. B. Long, B. C. Connelly, M. B. Colket, and R. J. Hall. Soot formation in laminar diffusion flames. *Combust. Flame*, 143:613–628, 2005. doi:10.1016/j.combustflame.2005.08.028.

[60] C. J. Sun, C. J. Sung, H. Wang, and C. K. Law. On the structure of nonsooting counterflow ethylene and acetylene diffusion flames. *Combust. Flame*, 107:321–335, 1996. doi:10.1016/S0010-2180(96)00055-7.

[61] J. Tauc, R. Grigorovici, and A. Vancu. Optical properties and electronic structure of amorphous germanium. *Phys. Stat. Sol.*, 15:627–637, 1966. doi:10.1002/pssb.19660150224.

[62] S. Tsantilis, H. Briesen, and S. E. Pratsinis. Sintering time for silica particle growth. *Aerosol Sci. Technol.*, 34:237–246, 2001. doi:10.1080/02786820119149.

[63] A. Violi. Modeling of soot particle inception in aromatic and aliphatic premixed flames. *Combust. Flame*, 139:279–287, 2004. doi:10.1016/j.combustflame.2004.08.013.

[64] H. Wang and M. Frenklach. A detailed kinetic modeling study of aromatics formation in laminar premixed acetylene and ethylene flames. *Combust. Flame*, 110: 173–221, 1997. doi:10.1016/S0010-2180(97)00068-0.

[65] R. H. West, R. A. Shirley, M. Kraft, C. F. Goldsmith, and W. H. Green. A detailed kinetic model for combustion synthesis of titania from $TiCl_4$. *Combust. Flame*, 156: 1764–1770, 2009. doi:10.1016/j.combustflame.2009.04.011.

[66] R. Whitesides and M. Frenklach. Detailed kinetic Monte Carlo simulations of graphene-edge growth. *J. Phys. Chem. A*, 114:689–703, 2010. doi:10.1021/jp906541a.

[67] E. K. Y. Yapp, D. Chen, J. Akroyd, S. Mosbach, M. Kraft, J. Camacho, and H. Wang. Numerical simulation and parametric sensitivity study of particle size distributions in a burner-stabilised stagnation flame. *Combust. Flame*, 162:2569–2581, 2015. doi:10.1016/j.combustflame.2015.03.006.

[68] J. Zerbs, K. P. Geigle, O. Lammel, J. Hader, R. Stirn, R. Hadef, and W. Meier. The influence of wavelength in extinction measurements and beam steering in laser-induced incandescence measurements in sooting flames. *Appl. Phys. B*, 96:683–694, 2009. doi:10.1007/s00340-009-3550-8.